

Frozen Mode in an Asymmetric Serpentine Optical Waveguide

Albert Herrero-Parareda, Ilya Vitebskiy, Jacob Scheuer, and Filippo Capolino*

The existence of a frozen mode in a periodic serpentine waveguide with broken longitudinal symmetry is demonstrated numerically. The frozen mode is associated with a stationary inflection point (SIP) of the Bloch dispersion relation, where three Bloch eigenmodes collapse on each other, as it is an exceptional point of order three. The frozen mode regime is characterized by vanishing group velocity and enhanced field amplitude, which can be very attractive in various applications including dispersion engineering, lasers, and delay lines. Useful and simple design equations that lead to realization of the frozen mode by adjusting a few parameters are derived. The trend in group delay and quality factor with waveguide length that is peculiar of the frozen mode is shown. The symmetry conditions for the existence of exceptional points of degeneracy associated with the frozen mode are also discussed.

of their diverse potential applications: loss-induced transparency, unidirectional invisibility, lasing-mode selection, lasing revivals and suppression, directional lasing, hypersensitive sensors, etc.^[3] The SIP scenario is also interesting and attractive because the frozen mode regime can be observed over a wide frequency range, ranging from RF,^[4,5] to optical frequencies.^[6–8] Moreover, third-order exceptional points of degeneracy (EPDs) have been found in a diverse range of structures: loss–gain balanced coupled-mode structures, such as PT-symmetric systems with glide symmetry.^[9,10] SIPs are found in periodic lossless and gainless coupled mode structures,^[6,11] periodic lossless and gainless gratings,^[12] and photonic

1. Introduction

The confinement and slowing down of light in photonic structures has gained interest in the past two decades due to its growing feasibility and possible applications. Of particular interest is the excitation of the frozen mode regime,^[1] where the wave transmitted inside a waveguide or in a supporting medium exhibits both vanishing group velocity and enhanced amplitude.^[2] The frozen mode regime is associated with a stationary inflection point (SIP) of the Bloch dispersion relation $\omega(k)$, where $\partial\omega/\partial k = 0$ and $\partial^2\omega/\partial k^2 = 0$ at $k = k_s$, where k_s is the SIP wavenumber. In this article, we focus on SIPs because


crystals.^[2] Furthermore, SIPs have been found in nonreciprocal structures, as shown in other studies,^[13–15] where the system becomes unidirectional near the SIP frequency.

One fundamental feature of the SIP-related frozen mode is that it corresponds to a particular third-order EPD, where three Bloch eigenmodes, one propagating and two evanescent, coalesce at the SIP frequency. For this to happen, all three Bloch eigenmodes collapsing on each other at the EPD must belong to the same 1D irreducible representation of the symmetry group G_k of the Bloch wavevector k .^[16] This requirement is quite different from the condition for the common symmetry-related degeneracy, where the degenerate eigenmodes must belong to the same multidimensional irreducible representation of G_k . As at any given frequency we have just a limited number of Bloch eigenmodes, the easiest way to automatically satisfy the above condition for the SIP existence is to have the symmetry of the waveguide as low as possible. We will apply this guiding principle when choosing the waveguide geometry. In a reciprocal periodic waveguide, there will be a pair of reciprocal SIPs with equal and opposite Bloch wavenumbers k . Therefore, the existence of EPD in a reciprocal waveguide requires at least six Bloch eigenmodes with the same symmetry, three coalescing Bloch eigenmodes in either direction. Here, we consider a specific example of asymmetric serpentine optical waveguide (ASOW) by applying symmetry-breaking distortion to the symmetric optical waveguide (SOW) in the study by Scheuer.^[17] This article is organized as follows. In Section 2, we describe the ASOW. In Section 3, we develop a transfer matrix formalism that facilitates obtaining the ASOW eigenmodes. In Section 4, we study the conditions for SIP existence. In Section 5, we analyze the scattering problem for a finite ASOW supporting a pair of reciprocal SIPs. In Section 6, we summarize the results.

A. Herrero-Parareda, F. Capolino
Department of Electrical Engineering and Computer Science
University of California, Irvine
Irvine, CA 92617, USA
E-mail: f.capolino@uci.edu

I. Vitebskiy
Air Force Research Laboratory
Sensors Directorate
Wright-Patterson AFB, OH 45433, USA

J. Scheuer
School of Electrical Engineering
Tel Aviv University
Ramat Aviv, Tel-Aviv 69978, Israel

 The ORCID identification number(s) for the author(s) of this article can be found under <https://doi.org/10.1002/adpr.202100377>.

© 2022 The Authors. Advanced Photonics Research published by Wiley-VCH GmbH. This is an open access article under the terms of the Creative Commons Attribution License, which permits use, distribution and reproduction in any medium, provided the original work is properly cited.

DOI: 10.1002/adpr.202100377

2. Geometry of the Asymmetric Serpentine Optical Waveguide

A SOW related to the one shown in this article was analyzed in the study by Scheuer et al.^[17] It was shown that that structure supported slow-light mode at regular band edges (RBE), where the group velocity vanishes. Instead, here we focus on a modification of that SOW structure, where the applied deformation and the lack of symmetry in each unit cell enable the occurrence of an SIP. As traditionally assumed^[18,19] and as in the study by Scheuer,^[17] we define the coupling as point-like and lossless, that is

$$\kappa^2 + \tau^2 = 1 \quad (1)$$

where κ and τ represent the field coupling and transmission coefficients, respectively. Both coefficients are constrained to $\kappa, \tau \in [0, 1]$.

The ASOW shown in **Figure 1** is a lossless periodic structure in which the adjacent loops are coupled to one another, allowing the formation of resonating optical paths. The waveguide in each unit cell is divided into three segments: A, B, and B'. Segment A is a quarter of a circle with radius R . In every unit cell there are two A segments at the top part, marked blue in **Figure 2**, and additional two A segments that form half of a circle at the bottom (also marked blue). Segment B is the left-side waveguide connecting the upper and bottom loops and depends directly on the radius R and α , marked in green. Segment B' on the right side of the unit cell is similar to segment B but it differs in that it depends on α' , as shown in orange in Figure 2. The local slope at the transition between top and bottom loops in Figure 2 is continuous because the intersection is between two arcs with the same radius R interconnecting at the same angle, either α or α' ; therefore, there is no slope discontinuity. The phase accumulation associated with each segment is given by

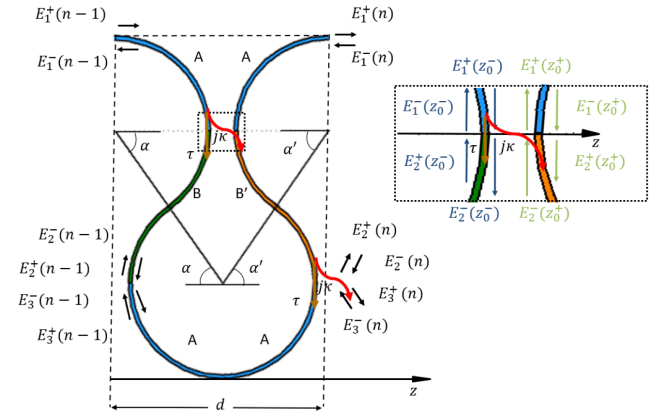


Figure 2. The n -th unit cell of the ASOW, with its boundaries represented by the two oblique dashed lines from the apex top of the upper loops at an angle $\beta = \alpha - \alpha'$ (the segment A of each top loop in the unit cell is exactly one-quarter of a circle). The unit cell waveguide is formed by three different segments A, B, B'. Segments A are quarters of a loop, marked in blue; Segment B is the waveguide that connects the upper loop with the bottom loop on the left, marked in green, and its length depends on the angle α ; and Segment B' is the waveguide that connects the bottom loop with the upper one, on the right, marked in orange and its length depends on α' . The dashed region on the top encloses the lumped, lossless, coupling point z_0 , which represents the point where the adjacent loops are the closest. Coupling exists also between the bottom loop and the two adjacent unit cells on the left and right (not depicted here).

$$\begin{aligned} \phi_a &= k_0 n_w \pi R / 2 \\ \phi_b &= k_0 n_w 2\alpha R \\ \phi'_b &= k_0 n_w 2\alpha' R \end{aligned} \quad (2)$$

where $k_0 = \omega/c$ is the wavenumber in vacuum, ω is the angular frequency, c is the speed of light in vacuum, R is the radius of the

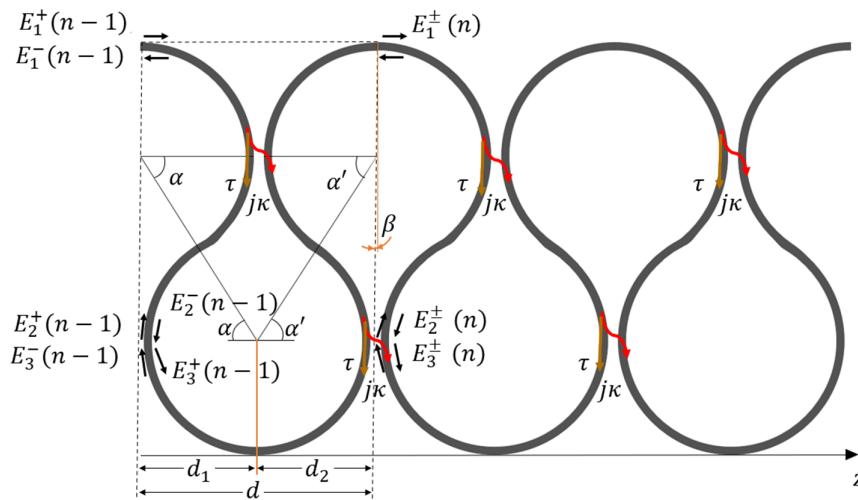


Figure 1. Periodic ASOW. The silicon waveguide follows a serpentine path. A unit cell of length d is defined within the two oblique dashed lines. These lines are defined from the apex of the top loops and at an angle $\beta = \alpha - \alpha'$ from the vertical. The lengths d_1 and d_2 are defined as the distance (at the bottom of the cell) between the dashed oblique lines and the vertical (nonoblique) orange line that goes from the center to the lowest point of the bottom loop. As $\alpha \neq \alpha'$, $d_1 \neq d_2$. The field amplitudes are defined to the right of the boundaries of the unit cell, with the sign of E_i^+ and E_i^- corresponding to the sign of the projection of the direction of propagation of that wave with the z -axis in the vicinity of the i -th port.

loops, and n_w is the effective refractive index of the waveguide's mode. α is the angle between the line that crosses the center of the top left and bottom loops and the horizontal axis. α' is the angle between the line that connects the centers of the bottom- and top-right loops and the horizontal axis. In this ideal design concept, we ignore the gaps between the waveguides in adjacent loops (gaps of the order of 50 – 100 nm) on the basis that they are significantly smaller than the radius of the loops (of the order of 10 μm). The precise gap size is decided based on the design of a realistic coupler; however, in this article for simplicity, each coupler is considered as “point like”, satisfying Equation (1). As such, the length of the unit cell is given by the diameter of the loops of the ASOW, $d = 2R$.

The key modification of the ASOW in this article with respect to the SOW in the study by Scheuer et al.^[17] is the difference between ϕ_b and ϕ_b' , which breaks the left-right (i.e., longitudinal) symmetry of the unit cell in terms of effective propagation length (akin to the misaligned anisotropic layers studied by Figotin et al.^[11]) and enables the formation of an SIP. The broken symmetry can be understood as a shear deformation as it is realized by imposing $\alpha \neq \alpha'$. The angle difference $\beta = \alpha - \alpha'$ assumed in this article to obtain an SIP is very small, so the difference in the lengths of segment B and B' is barely noticeable in Figure 2. In Figure 1, β is the angle between the dashed oblique line that defines the boundary at the right side of the unit cell and the vertical orange line crossing the center of the bottom loop and its lowest point.

3. Transfer Matrix Formalism

We model the electromagnetic guided fields in terms of forward E_i^+ and backward waves E_i^- , with $i = 1, 2, 3$, where the superscripts denote the sign of the projection of the direction of propagation of the wave on the z -axis. The time convention $e^{j\omega t}$ is implicitly assumed.

The unit cell has six ports, with E_1^+ , E_2^+ , and E_3^+ propagating toward the right and E_1^- , E_2^- , and E_3^- propagating toward the left (at or in the vicinity of the ports). The fields are defined at the right of the boundaries. We assume the coupling between adjacent loops to be lumped and lossless. The scattering matrix relating the incoming and outgoing fields at the coupling point z_0 is defined in Appendix A and shown in Figure 2.

We define a state vector with all the six electric field wave amplitudes as

$$\Psi(n) = (E_1^+, E_1^-, E_2^+, E_2^-, E_3^+, E_3^-)^T \quad (3)$$

where n denotes the unit cell number, as shown in Figure 1 and 2. The six field terms are calculated at the right side of the same cell, and T denotes the transpose operator. Note that this definition has terms arranged differently from those used by Nada et al.^[6] and it is the same used in the study by Scheuer,^[17] albeit with a different notation. The state vector on the right side of the n -th unit cell is $\Psi(n)$. Its “evolution” along the periodic ASOW is described by

$$\Psi(n) = \underline{T}_u \Psi(n-1) \quad (4)$$

where \underline{T}_u is the 6×6 transfer matrix of the unit cell of the ASOW. As the ASOW is reciprocal, the determinant of the transfer matrix satisfies $\det(\underline{T}_u) = 1$, which causes the eigenvalues of this matrix to come in three reciprocal pairs. This causes the dispersion diagram to show the symmetry that if $k(\omega)$ is a solution of (8), then also $-k(\omega)$ is. Hence, the dispersion diagram is symmetric with respect to the center of the Brillouin zone (BZ), defined here with $\text{Re}(k)$ from $-\pi/d$ to π/d . The transfer matrix of the unit cell is given by

$$\underline{T}_u = \begin{pmatrix} 0 & -j\frac{\tau}{\kappa} & j\frac{e^{j(\phi_a+\phi_b)}}{\kappa} & 0 & 0 & 0 \\ j\frac{\tau}{\kappa} & 0 & 0 & -j\frac{e^{-j(\phi_a+\phi_b)}}{\kappa} & 0 & 0 \\ 0 & -\frac{\tau e^{-j(\phi_a+\phi_b')}}{\kappa^2} & \frac{\tau^2 e^{j(\phi_b-\phi_b')}}{\kappa^2} & 0 & j\frac{e^{j2\phi_a}}{\kappa} & 0 \\ -\frac{\tau e^{j(\phi_a+\phi_b')}}{\kappa^2} & 0 & 0 & \frac{\tau^2 e^{-j(\phi_b-\phi_b')}}{\kappa^2} & 0 & -j\frac{e^{-j2\phi_a}}{\kappa} \\ -\frac{e^{-j(\phi_a+\phi_b')}}{\kappa^2} & 0 & 0 & \frac{\tau e^{-j(\phi_b-\phi_b')}}{\kappa^2} & 0 & -j\frac{\tau e^{-j2\phi_a}}{\kappa} \\ 0 & -\frac{e^{-j(\phi_a+\phi_b')}}{\kappa^2} & \frac{\tau e^{j(\phi_b-\phi_b')}}{\kappa^2} & 0 & j\frac{\tau e^{j2\phi_a}}{\kappa} & 0 \end{pmatrix} \quad (5)$$

Its calculation is shown in Appendix A. Note that if $\phi_b = \phi_b'$, this transfer matrix reduces to that of the SOW in the study by Scheuer et al.,^[17] where the lossless coupling relation shown in Equation (1) was defined in units of power instead of units of field amplitude used in this article.

From the Bloch theorem,^[20] which states that the field at each unit cell is determined by the field at the adjacent one and a unit cell phase shift, we obtain

$$\Psi(n) = e^{-jkd} \Psi(n-1) \quad (6)$$

where k is the Bloch wavenumber of a guided eigenmode and d is the length of the unit cell. Using (4) and (6), we write the eigenvalue problem

$$\underline{T}_u \Psi(n-1) = \zeta \Psi(n-1) \quad (7)$$

where $\zeta = e^{-jkd}$. Solving it gives us the eigenvalues and the eigenvectors of the system. When three of these eigenmodes coalesce to a degenerate one with $\text{Re}(k) \neq 0$, the SIP is formed, which is an EPD of order three. The eigenvalue solutions are found from the characteristic equation

$$D(k, \omega) \equiv \det(\underline{T}_u - \zeta \underline{I}) = 0 \quad (8)$$

After some algebraic manipulation, we arrive at the following characteristic polynomial

$$\begin{aligned}
 D(k, \omega) = & \zeta^6 - \zeta^5 \left(2 \frac{\tau^2}{\kappa^2} \cos(\phi_b - \phi'_b) \right) + \zeta^4 \left(-2 \frac{\tau^2}{\kappa^2} + \frac{\tau^4}{\kappa^4} \right) \\
 & - \zeta^3 \left(\frac{2 \cos(4\phi_a + \phi_b + \phi'_b)}{\kappa^4} + \frac{4(\tau^2 - \tau^4) \cos(\phi_b - \phi'_b)}{\kappa^4} \right) \\
 & - \zeta^2 \left(-\frac{\tau^4}{\kappa^4} + 2 \frac{\tau^6 - 2\tau^4 + \tau^2}{\kappa^6} \right) \\
 & - \zeta \left(2 \frac{\tau^6 - 2\tau^4 + \tau^2}{\kappa^6} \cos(\phi_b - \phi'_b) \right) \\
 & + \frac{\tau^8 - 4\tau^6 + 6\tau^4 - 4\tau^2 + 1}{\kappa^8}
 \end{aligned} \quad (9)$$

The difference between ϕ_b and ϕ'_b is manifested only inside the cosine function, which is an even function. As such, interchanging the values of ϕ_b and ϕ'_b does not change the spectral properties of the ASOW. Notice that due to reciprocity of the ASOW, the solutions come in reciprocal pairs: k_1 and $-k_1$, k_2 and $-k_2$, and k_3 and $-k_3$. In other words, if ζ is an eigenvalue, $1/\zeta$ is an eigenvalue as well. In the following we represent the wavenumbers in the first BZ, defined here with its center at $\text{Re}(k) = 0$. Because of periodicity, a solution $-k_i$ has Floquet harmonics of the form $-k_i + 2\pi m/d$, where m is any integer number. The transfer matrix of the unit cell is similar to the diagonal matrix

$$\underline{T}_u = \underline{V} \underline{\Lambda} \underline{V}^{-1} \quad (10)$$

where $\underline{V} = [\psi_1 | \psi_2 | \psi_3 | \psi_4 | \psi_5 | \psi_6]$ is the similarity matrix transformation with eigenvectors ψ_i as columns, and

$$\underline{\Lambda} = \begin{pmatrix} e^{-jk_1 d} & 0 & 0 & 0 & 0 & 0 \\ 0 & e^{-jk_2 d} & 0 & 0 & 0 & 0 \\ 0 & 0 & e^{-jk_3 d} & 0 & 0 & 0 \\ 0 & 0 & 0 & e^{jk_1 d} & 0 & 0 \\ 0 & 0 & 0 & 0 & e^{jk_2 d} & 0 \\ 0 & 0 & 0 & 0 & 0 & e^{jk_3 d} \end{pmatrix} \quad (11)$$

is the diagonal matrix with the eigenvalues ζ_i , with $i = 1, \dots, 6$.

4. Exceptional Points of Degeneracy

EPDs are defined as the points where the eigenmode orthogonality collapses, which means that the algebraic multiplicity of an eigenvalue (the number of identical roots of the characteristic polynomial) is higher than the geometric multiplicity (the number of independent eigenvectors associated with that eigenvalue). This dissonance causes the matrix to not be diagonalizable and it is similar to a matrix containing at least a nontrivial Jordan block. The number of coalesced eigenvectors gives the order of the EPD, with the SIP being an EPD of third order.

Given the reciprocity of the ASOW, which is seen as a three-way waveguide (analogously to those in Refs. [4,6,7,21]), this waveguide supports at any given frequency three pairs of reciprocal Bloch eigenmodes, which allow only degeneracies of order 2, 3, 4, and 6 to form. For the ASOW to exhibit an SIP at a generic point, that is, away from the center or the boundaries of the BZ, all three Bloch eigenmodes with the same sign of $\text{Re}(k)$ should coalesce. In the case of the undistorted SOW, the symmetry of a

generic point of the BZ has a single nontrivial operation, the glide mirror plane normal to the x -direction. Any Bloch eigenmode, propagating or evanescent, of the undistorted structure is either even or odd with respect to the above symmetry operation. Normally, two of the three eigenmodes have the same parity, while the third one has the opposite parity. The states with the opposite parity do not usually coalesce and, thus, are less likely to participate in SIP formation. On the other hand, the two eigenmodes with the same parity can coalesce and form RBE.^[17] To facilitate the coalescence of all three eigenmodes of $\text{Re}(k)$ with the same sign, we break the glide plane symmetry by applying the shear distortion described in Figure 1 on the undistorted SOW.

In this article, we focus on finding SIPs, which are found as inflection points at (k_s, ω_s) in the dispersion diagram, locally approximated as

$$\omega - \omega_s \propto (k - k_s)^3 \quad (12)$$

The existence of an SIP indicates that the structure (ASOW in our case) possesses a frozen mode regime, exhibiting huge diverging amplitudes and low group velocity.^[1] At frequencies in the vicinity of the SIP, the guided field is a superposition of a propagating and two evanescent Bloch modes, which develop strong singularity close to the SIP frequency while remaining nearly equal and opposite in sign at the boundary of the structure, satisfying boundary conditions (BCs).

The advantage of the SIP compared with EPDs of even order such as RBE and degenerate band edge, or DBE (order 2 and 4, respectively), is that it can exhibit a good coupling efficiency,^[12] with a significant fraction of the incident light coupling into the waveguide. The high coupling efficiency allows SIP-exhibiting structures to interact effectively with external devices. This is in contrast to structures exhibiting RBEs and DBEs where the impedance mismatch is substantially larger.^[22]

An SIP is defined as a third-order EPD, which means that (10) does not hold anymore and that \underline{T}_u is degenerate with two reciprocal eigenvalues of algebraic multiplicity 3 and geometric multiplicity 1 (i.e., there are only two eigenvalues $\zeta_s = e^{-jk_s d}$ and $\zeta_s^{-1} = e^{jk_s d}$, repeated three times each, and two eigenvectors associated with those eigenvalues).

4.1. Analytic Dispersion Relation for an SIP

We derive analytically the system of equations that constraint the values of the ASOW parameters κ , R , α , and α' such that the ASOW exhibits an SIP. At the SIP angular frequency ω_s the characteristic equation of the system, found in Equation (8), can be cast in a simple way because it has two degenerate Floquet–Bloch eigenwaves. Hence, the characteristic equation evaluated at ω_s must have the form

$$D(k, \omega_s) = (\zeta - \zeta_s)^3 (\zeta - \zeta_s^{-1})^3 = 0 \quad (13)$$

By equating the coefficients of this polynomial with those of the dispersion relation in Equation (9) evaluated at ω_s , we derive the following five necessary conditions.

$$\begin{aligned}
 2 \frac{\tau^2}{\kappa^2} \cos(\phi_b - \phi'_b) &= 3(\zeta_s + \zeta_s^{-1}), \\
 2 \cos(4\phi_a + \phi_b + \phi'_b) + 4(\tau^2 - \tau^4) \cos(\phi_b - \phi'_b) &= \\
 \frac{\kappa^4}{\kappa^4} &= (\zeta_s^3 + \zeta_s^{-3}) + 9(\zeta_s + \zeta_s^{-1}), \\
 2 \frac{(\tau^6 - 2\tau^4 + \tau^2) \cos(\phi_b - \phi'_b)}{\kappa^6} &= 3(\zeta_s + \zeta_s^{-1}), \\
 \frac{\tau^4}{\kappa^4} - 2 \frac{\tau^6 - 2\tau^4 + \tau^2}{\kappa^6} &= 3(\zeta_s^2 + \zeta_s^{-2}) + 9 \\
 \frac{\tau^8 - 4\tau^6 + 6\tau^4 - 4\tau^2 + 1}{\kappa^8} &= 1
 \end{aligned} \tag{14}$$

Equation (14) must be satisfied for the ASOW to exhibit an SIP at ω_s . The last equation is automatically verified when the coupling and transmission coefficients satisfy Equation (1), that is, when each coupling is lossless. The fourth equation does not depend on ϕ_a , ϕ_b , and ϕ'_b , and the choice of the coupling and transmission coefficients determines the value of ζ_s and hence the wavenumber k_s of the SIP. The first and the third are not independent: after equating their right hand sides, we get an equation in τ and κ only, which is verified assuming that the coupling and transmission satisfy Equation (1). Therefore, either the first or the third equation is useful to determine the phase difference $\phi_b - \phi'_b$ once the coupling and transmission coefficients have been determined. The second equation is useful to determine the phase term $4\phi_a + \phi_b + \phi'_b$, which is the total phase accumulated in a unit cell when we do not consider coupling effects. This shows that there are various combinations of the lengths of the segments A, B, and B' that lead to an SIP.

To quantify the coalescence of the eigenvectors, we use the concept of “coalescence parameter” introduced in the study by Abdelshafy et al.^[23] for the DBE and in the study by Nada et al.^[4] for the SIP. Here, we use a coalescence parameter σ defined similarly to that in the study by Nada et al.,^[4] as

$$\begin{aligned}
 \sigma &= \sqrt{\sigma'^2 + \sigma''^2} \\
 \sigma' &= \sqrt{\sum_{m=1, n=2, n>m}^3 |\theta_{mn}|^2} \\
 \sigma'' &= \sqrt{\sum_{m=4, n=5, n>m}^6 |\theta_{mn}|^2} \\
 \cos(\theta_{mn}) &= \frac{|\langle \Psi_m | \Psi_n \rangle|}{\|\Psi_m\| \|\Psi_n\|}
 \end{aligned} \tag{15}$$

The coalescence parameter is calculated by organizing the eigenvectors Ψ_i in two sets of three vectors, associated with ζ_i and $1/\zeta_i$, respectively, with $i = 1, 2, 3$. Then, we calculate the Euclidean distance of the angles between all the combinations in the set with respect to the origin. Here, θ_{mn} is the angle between two six-dimensional complex vectors Ψ_m , Ψ_n , which is defined as stated in Equation (15) using the inner product $\langle \Psi_i | \Psi_j \rangle = \Psi_i^\dagger \Psi_j$ with the dagger symbol \dagger representing the complex conjugate transpose operation and $\|\Psi_m\|$ denotes the norm of Ψ_m .^[4] In this article, we calculate the coalescence parameter using the norm based on the Euclidean distance between the parameters θ_{mn} , $\forall m, n$, and zero,^[23] instead of using the

arithmetic average used in.^[4,24] The reason for this change is that the optimization algorithm converges faster using the Euclidean distance than the arithmetic average, as long as the algorithm does not generate a lot of points far from the optimization goal (known as outliers).^[25] The coalescence parameter is always positive and smaller than 1, with $\sigma = 0$ (the origin) indicating the perfect coalescence of each set of three eigenvectors. This point constitutes an SIP.

4.2. ASOW with SIP

In this section we show that the proposed ASOW exhibits an SIP through the proper tuning of the various structure parameters. For practical purposes, the SIP wavelength is set at 1550 nm; the waveguide consists of a silicon-over-insulator structure, and the Si waveguide is assumed to have a height of 230 nm and a width of 430 nm. At this wavelength, the lowest TE-like mode has an effective refractive index of $n_w = 2.362$, as can be seen in the study by Scheuer et al.^[17] In the study by Dattner et al.,^[26] it is also seen that the variation of the refractive index is negligibly small in the frequency range of interest. In order for the assumption that the structure is lossless at optical frequencies to be reasonable, we restrict ourselves to ASOWs comprising loops with radius $R \geq 10 \mu\text{m}$ ^[27] to minimize radiation losses.

Figure 3 depicts the dispersion diagram of the eigenmodes of the ASOW unit cell shown in Figure 1. It exhibits an SIP that can be seen by the coalescing of the three branches in both the real and imaginary parts.

In addition to the SIP, we also find an RBE not far from the SIP. The distance between the RBE and the SIP most likely decreases with an increasing loop radius. The reasoning behind it is that a larger radius causes the structure to support multiple resonances and reduces its free spectral range, although more work has to be done to investigate how to design RBEs far from the SIP. The fact that both RBEs and SIPs are both found in a small frequency range could be problematic when realizing lasers. Therefore, learning how to optimize the size of the loops to balance between bending (radiation) losses and the formation of RBEs near the SIP frequency is important for exploiting the potential of an SIP.

5. Analysis of a Finite-Length Structure

We analyze an ASOW with a finite length $L = dN$, where d is the period of the unit cell and N is the number of unit cells. This finite-length structure is shown in Figure 4.

5.1. Field Amplitudes Along the ASOW

The evolution of the field amplitudes from one unit cell to the next is given by Equation (4). To find the field amplitudes at each unit cell of the structure shown in Figure 4, we need to find the field amplitudes (i.e., the state vector) at either end of the structure.

We consider the state vector at the left boundary of the first unit cell of the structure, $\Psi_0 = \Psi(n = 0)$. The state vector at the end of the ASOW made of N cascaded unit cells is given by

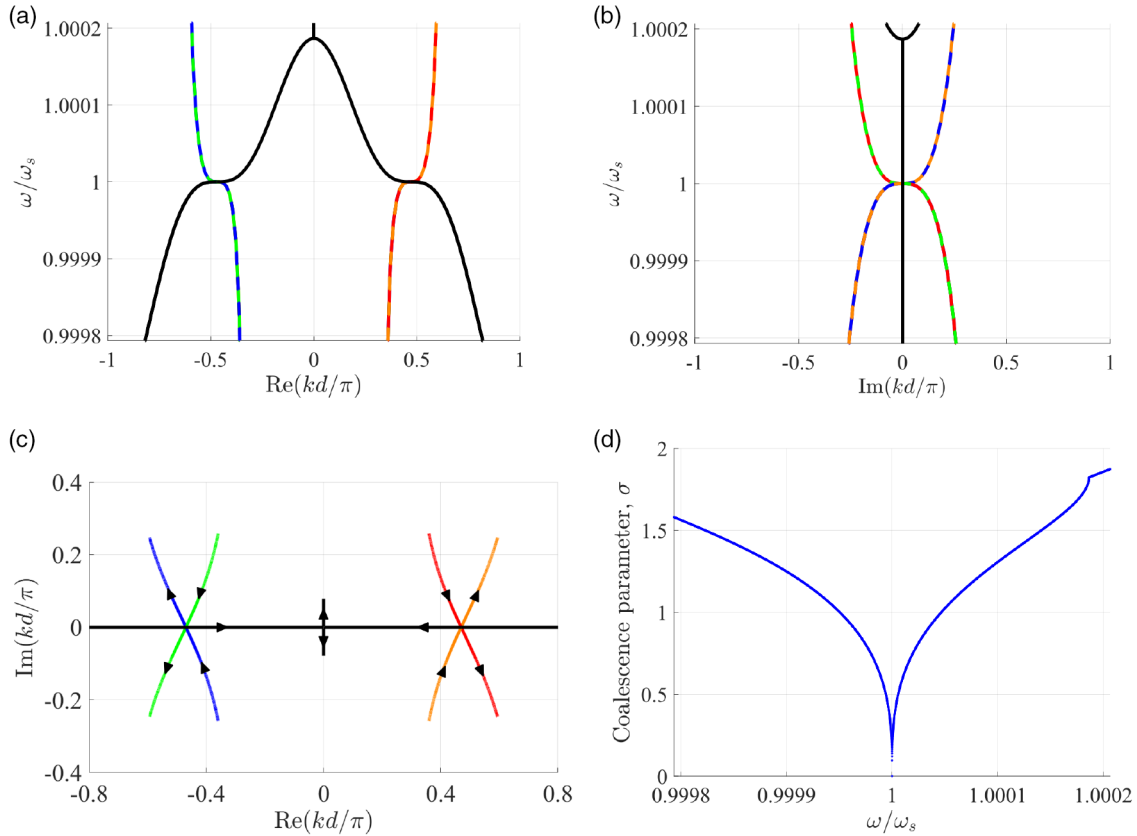


Figure 3. Modal dispersion diagram showing the formation of an SIP, using structure parameters $R = 10 \mu\text{m}$, $\alpha = 66.02^\circ$, $\alpha' = 56.18^\circ$, and $\kappa = 0.49$. a) Real part of the wavenumber versus angular frequency in the fundamental BZ. Solid black: mode with purely real k ; dashed colors: modes with complex k (overlapping dashed colors imply two overlapping branches). It is clear that three curves meet at an inflection point, with reciprocal k and $-k$ positions. b) Imaginary part of k versus angular frequency. At the SIP, $\text{Im}(k) = 0$. c) Alternative representation of the dispersion diagram in the complex k space. The coalescing of the three branches is clearer in this figure, with arrows pointing in the direction of increasing frequency. d) Coalescence parameter σ versus angular frequency, with σ vanishing at the SIP frequency.

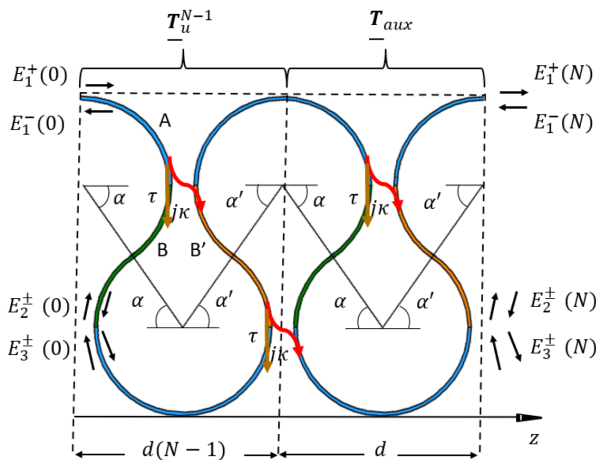


Figure 4. Schematic of a finite-length ASOW consisting of N unit cells, most of which are described by the transfer matrix \mathbf{T}_u^{N-1} and a last unit cell without the second coupling, which connects the ports 2 and 3 as defined in Figure 2. This last unit cell is described by the transfer matrix \mathbf{T}_{aux} and has a length d , as we neglect the gap between adjacent loops. All the units cells are defined within parallel oblique dashed lines as described in Section 2.

$$\Psi(N) = \mathbf{T}\Psi_0 \quad (16)$$

Dividing the ASOW in unit cells as shown in Figure 4, we find that

$$\mathbf{T} = \mathbf{T}_{aux} \mathbf{T}_u^{N-1} = \mathbf{T}_{aux} \mathbf{V} \mathbf{\Lambda}^{N-1} \mathbf{V}^{-1} \quad (17)$$

where \mathbf{T}_{aux} is the transfer matrix of a unit cell without the second coupling point and it is given in Appendix. The diagonal matrix $\mathbf{\Lambda}$ is defined as in Equation (10). At an SIP, the transfer matrix is nondiagonalizable and similar to a matrix containing two Jordan blocks.^[6]

We assume the ASOW is excited by an incoming wave $E_1^+(0) = E_{inc}$ from the left, and the right end is terminated on a dielectric waveguide with the same shape and characteristic impedance of the waveguide used to form the ASOW. Considering the definitions in Figure 4, the fields defining the BCs of the waveguide are

$$\begin{aligned}
 E_1^+(0) &= E_{inc} \\
 E_1^-(N) &= 0 \\
 E_2^+(0) &= E_3^-(0) \\
 E_3^+(0) &= E_2^-(0) \\
 E_2^-(N) &= E_3^+(N) \\
 E_3^-(N) &= E_2^+(N)
 \end{aligned} \tag{18}$$

Applying these BCs to the state vector “evolution” described in Equation (16) gives the field amplitudes at either side of the boundary. By applying Equation (4), we obtain the field amplitudes at each unit cell from those at $n = 0$. The results for $|E_1^+(n)|$, $|E_1^-(n)|$, and $|E_1(n)|$ over $n \in [0, N]$ are shown in **Figure 5** where $N = 32$. The frozen mode regime, which is characteristic of light traveling with null group velocity followed by a dramatic enhancement of the field amplitudes,^[2] is in full display. The amplitudes of the fields in the middle of the finite-length structure are substantially larger than those located at its edges, where the BCs shown in Equation (18) are satisfied. This frozen mode regime is visible in the magnitude of both the forward and backward waves, as shown in Figure 5, where $|E_1^+(n)|$, $|E_1^-(n)|$, and their sum $|E_1(n)| = |E_1^-(n) + E_1^+(n)|$ peak around the center of the finite-length waveguide.

5.2. Transfer Function

Besides the spatial evolution of the field amplitudes along the finite-length structure, we are interested in finding the proportion of light that makes it through the waveguide and the proportion of light that is reflected from it. We define the transfer function

$$T_f = \frac{E_{out}}{E_{inc}} = \frac{E_1^+(N)}{E_1^+(0)} \tag{19}$$

as the ratio between the forward field amplitude at the output of the ASOW and the incident one. We also define the reflection function

$$R_f = \frac{E_{refl}}{E_{inc}} = \frac{E_1^-(0)}{E_1^+(0)} \tag{20}$$

as the ratio between the backward field amplitude at the input of the ASOW and the incident one. The transfer function is equivalent to the s -parameter S_{21} and R_f is equivalent to S_{11} .

Figure 6 and **7** respectively show the magnitude of the transfer and the reflection functions (in dB) of ASOW comprising N -cascaded unit cells, for several values of N . The parameters of the structure are chosen to satisfy the conditions from Equation (14) to exhibit the SIP shown in Figure 3.

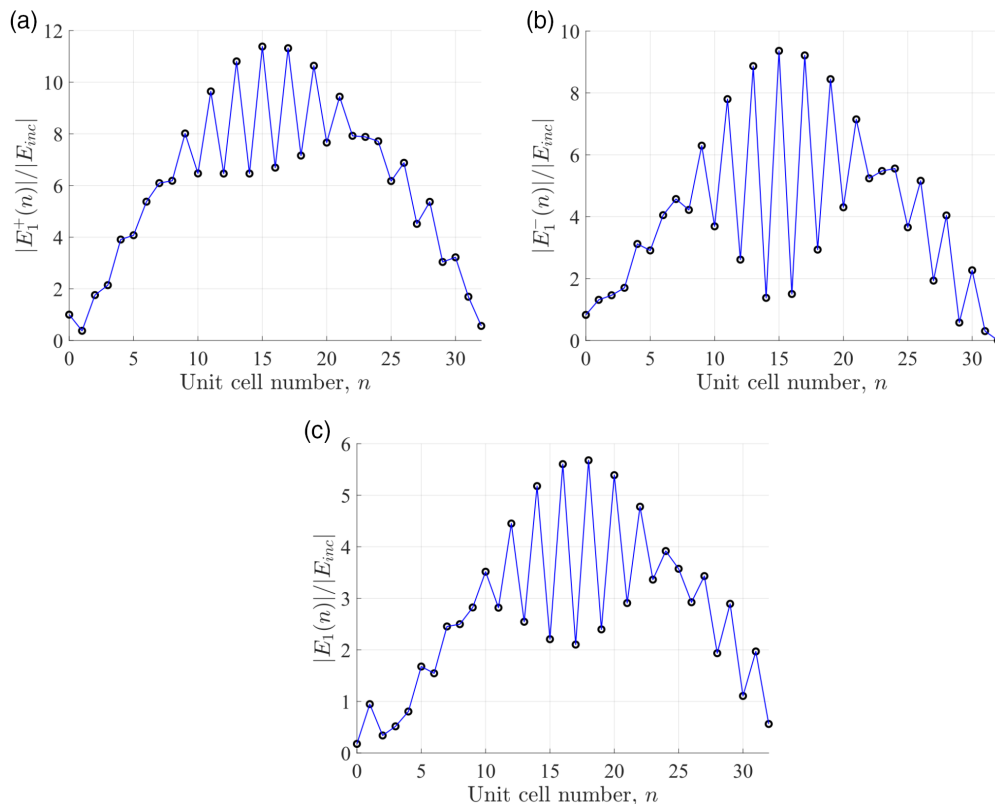


Figure 5. Magnitude of the forward and backward fields throughout the SIP-exhibiting finite-length structure against the position of the unit cell, with $n \in [0, N]$ for $N = 32$ at the SIP frequency ω_s . Notice that the BCs from Equation (18) are satisfied. a) Magnitude of $E_1^+(n)$ for $n \in [0, N]$. b) Magnitude of $E_1^-(n)$ for $n \in [0, N]$. c) Magnitude of $E_1(n) = E_1^-(n) + E_1^+(n)$ for $n \in [0, N]$.

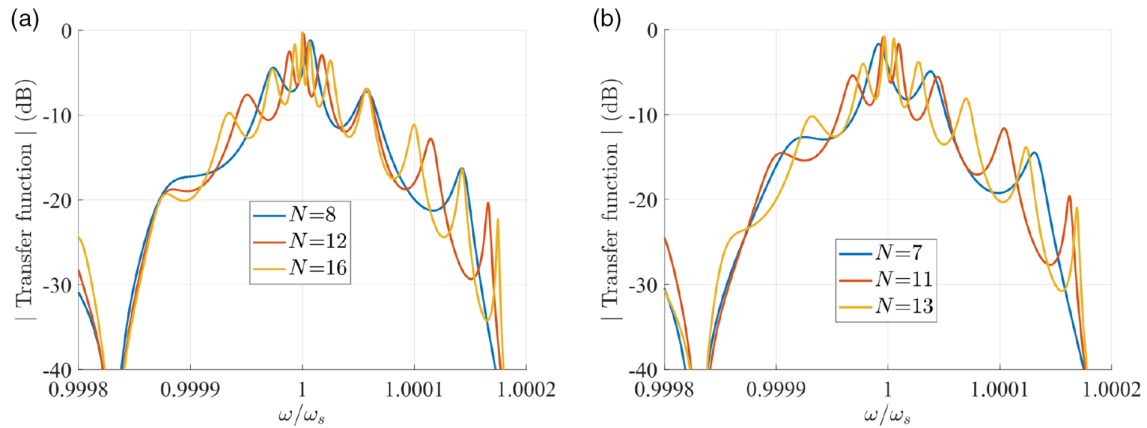


Figure 6. Magnitude of the transfer function (in dB) of the finite-length structure near the SIP frequency for a) even and b) odd number of unit cells N .

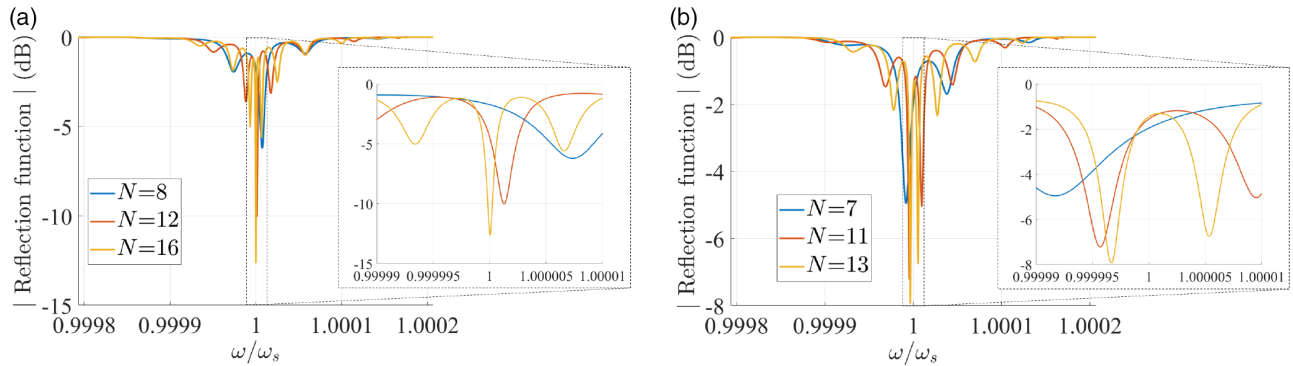


Figure 7. Magnitude of the reflection function (in dB) of the finite-length structure near the SIP frequency for a) even and b) odd number of unit cells N .

The transmission curves reach their maximum in the vicinity of the SIP frequency, where the reflection curves reach their minimal level. The resonance closest to the SIP frequency is denoted hereon as SIP resonance. The distance between peaks in each curve shrinks as N increases. Notice that the peaks in Figure 6a for even N are more bundled together around the SIP frequency ω_s than for odd N .

5.3. Group Delay and Quality Factor

The quality factor (Q) of a cavity is a measure of the energy lost per cycle versus the energy stored in the cavity. Very large Q factors in the vicinity of SIPs originate from the combination of the frozen mode regime and the common slow-wave resonance.^[1] Nevertheless, at EPDs other than the SIP (i.e., the DBE), systems can be highly mismatched to the termination impedance of most loads. This phenomenon stems from the Floquet–Bloch impedance^[22] in a multi-TL and causes an EPD-exhibiting structure to act as an isolated cavity. This is especially true for the case of DBEs.^[28] The ASOW does not behave as a very high- Q resonator at the SIP frequency as the frozen mode regime is not a cavity resonance.^[1,11]

The Q factor, however, does depend on the particular design of the SIP and its Bloch impedance. In the following we calculate the quality factor as

$$Q = \frac{\omega_{\text{res}} \tau_g}{2} \quad (21)$$

that provides a very good approximation for high-quality factors.^[6] Here, ω_{res} is the SIP resonance (the angular frequency corresponding to the closest peak to the SIP frequency) and τ_g is the group delay at that frequency. As the range of frequencies we operate in is small, the resonant frequency ω_{res} is approximately the same for all the group delay peaks in Figure 8. The group delay is calculated as the negative of the derivative of the phase of the transfer function with respect to the angular frequency, that is

$$\tau_g = -\frac{\partial \angle T_f}{\partial \omega} \quad (22)$$

Figure 8 shows the group delay versus angular frequency for structures with different number of unit cells, N .

It is normalized by the baseline delay

$$\tau_0 = N \frac{n_w}{c} (2\pi R + 2(\alpha' + \alpha)R) = N\tau'_0 \quad (23)$$

that occurs in a finite-length structure with the same length as the ASOW, without considering the couplings (i.e., without frozen mode). For the SIP-exhibiting ASOW from Section 4, which had $R = 10 \mu\text{m}$, $\alpha = 66.02^\circ$, and $\alpha' = 56.18^\circ$, we have

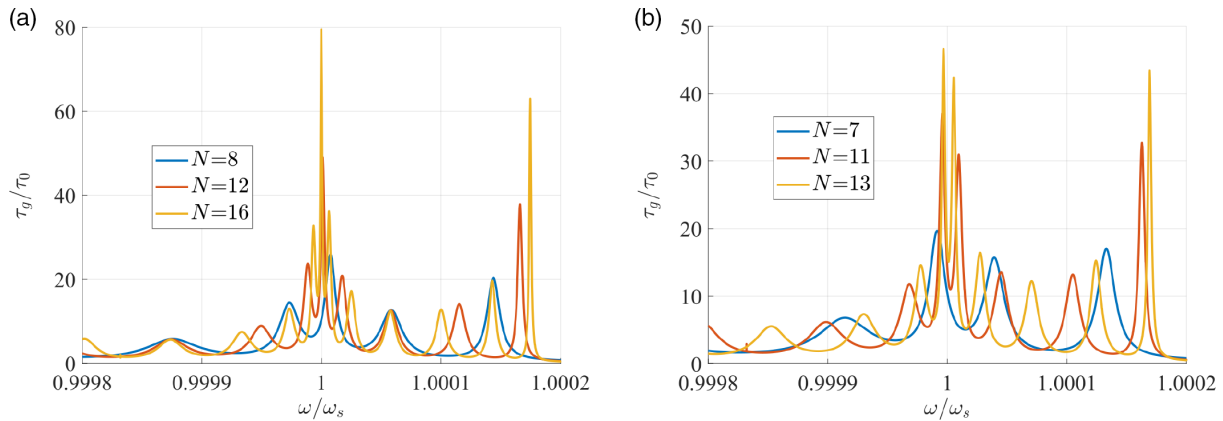


Figure 8. Normalized group delay versus normalized frequency for different number of unit cells N for a) even number of unit cells N and b) odd number of unit cells.

$\tau'_0 = 0.83$ ps. In Figure 8 we can see the normalized group delay. As expected, for frequencies below the SIP frequency, τ_g approximates τ_0 , although it does not quite reach that low value because τ_0 does not take into account the resonant paths enabled by the existence of the coupling points. For frequencies above the RBE frequency, which is the frequency at which the ASOW exhibits an RBE, $\tau_g \rightarrow 0$, as there is no propagation through the waveguide and the field experiences an exponential decay while propagating inside the waveguide because of the bandgap in the dispersion diagram in Figure 3.

In Figure 9, we plot the quality factor Q versus the number of unit cells N of the ASOW in Figure 4. The two plots are for even (a) and odd (b) numbers N . In both cases, Q grows with the number of unit cells following the trend $Q \propto b_e N^3$ for large N .^[1] The proportionality constants b_e and b_o for the even and odd N cases are different from each other, with $b_e = 128.9$ and $b_o = 99.8$. The fitting curve shown in Figure 9 is $Q = 128.9 N^3 - 5354$ for an even number of unit cells. For ASOWs with an odd number of unit cells, $Q = 99.8 N^3 + 3.2 \times 10^4 N - 3.4 \times 10^5$. Both fittings are done with $N \in [20, 50]$. The high-quality factors in

the figures in Figure 9 occur because the model of the ASOW does not take into account radiation or scattering losses.

Despite the growing trend of Q with N , the frequency at which the Q is maximum does not necessarily get monotonically closer to the SIP frequency, as shown in Figure 8 looking at the group delay peaks. Moreover, for a relatively small number of unit cells, with $N \in [10, 20]$, ASOWs with an even number of unit cells have a higher Q than ASOWs with odd N of comparable length, suggesting a stronger cavity-like behavior for ASOWs with even N . This is seen in Figure 9. For larger N , this difference disappears.

Figure 8 shows the normalized group delay peaks in the vicinity of the SIP frequency and near the RBE frequency, indicating that Q is higher near EPD frequencies. As mentioned before, the Q around the SIP frequency grows as $Q_{\text{SIP}} = b_{\text{SIP}} N^3$. Note that also for the resonances near the RBE, we have the asymptotic trend $Q_{\text{RBE}} = b_{\text{RBE}} N^3$ as discussed in other studies.^[1,28] For the ASOW considered here, the Q in the vicinity of the SIP frequency is comparable with Q in the vicinity of the RBE. This occurs even though the SIP displays a frozen mode regime and has a higher degeneracy order than the RBE.

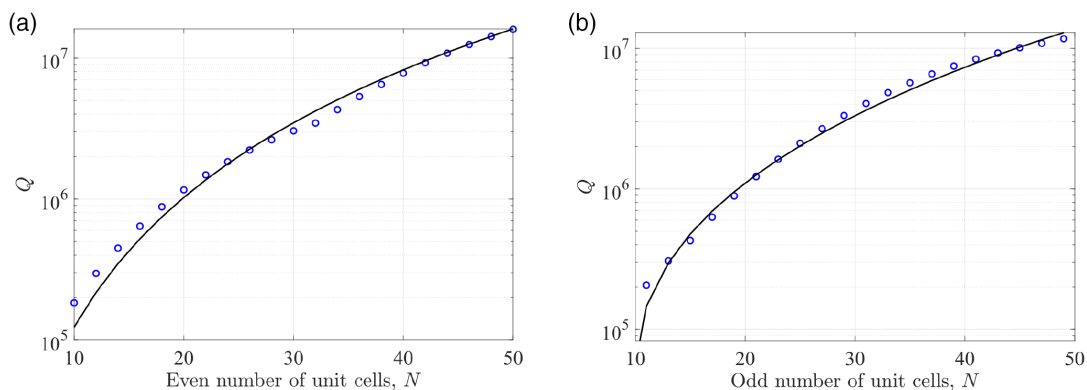


Figure 9. Quality factor versus number of unit cells N of the finite-length structure for a) even-number N , where Q evolves as $b_e N^3$, and b) odd-number N , where Q evolves as $b_o N^3$, with $b_e \neq b_o$.

As the SIP exhibits high transmittance, it allows a balance between the dramatic enhancement of the field amplitudes associated with an exceptional point and the low coupling to external waveguides due to mismatch. A high level of mismatch is instead typically found in DBEs, which have a higher quality factor scaling law.^[6] In Gutman et al.,^[12] it is shown that SIP-exhibiting structures have a high coupling coefficient, with a significant part of the incident light being transmitted into the frozen mode regime. This feature reduces the Q factor of the structure and the cavity-like properties that, instead, band edges usually exhibit. As such, SIP-exhibiting structures can be devised to realize unidirectional lasers^[13] that are otherwise not suitable with waveguides with an even-order EPD, such as an RBE or a DBE,^[29] which are used to form high Q cavities with low transmittance.

6. Conclusion

We have demonstrated that a lossless ASOW can support a pair of reciprocal SIPs associated with the frozen mode regime. The SIP has been obtained using the extra degree of freedom by applying shear distortion that breaks the glide symmetry of the original symmetric SOW. Our formulation explicitly reveals that the SIP is an exceptional point of third order in a lossless/gainless waveguide. To show that, we resort to the concept of “coalescence parameter” whose vanishing value reveals the coalescence of three eigenvectors, explicitly demonstrating that the SIP is indeed a third-order exceptional point of degeneracy. The study of finite-length waveguides shows the field enhancement and a large group delay at Fabry–Perot resonances near the SIP frequency. We have also studied the evolution of the transfer and reflection functions in the vicinity of the SIP, varying the length of the waveguide cavity and revealing the cubic-length scaling of the quality factor. High transmission is observed, shown by a transfer function nearing 0 dB close to the SIP frequency, with a reasonably high-quality factor, allowing for matching the SIP-exhibiting structure to external devices. Periodic waveguides supporting the SIP-related frozen mode regime can be used for cavityless light amplification and lasing, optical sensors, microwave and optical modulators, and switches.

Appendix

In this appendix we show how to obtain the transfer matrix of the unit cell of the ASOW \underline{T}_u and the auxiliary matrix \underline{T}_{aux} , which is akin to \underline{T}_u without modeling the second coupling point. The state vector is given in Equation (3).

As the unit cell of the structure has different resonant paths, the transfer matrix for the unit cell cannot be calculated in one step. Instead, we break the unit cell into several segments shown in Figure A1.

We call \underline{T}_{1c} and \underline{T}_{2c} the transfer matrices that model the relations between field amplitudes on either side of the infinitesimal segments (in z) that include the coupling points. The transfer matrices \underline{T}_{1p} and \underline{T}_{2p} account for phase accumulation in the segments of the unit cell.

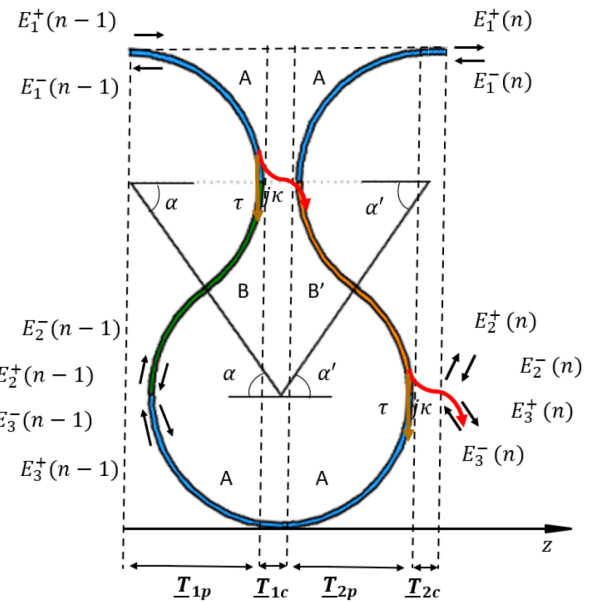


Figure A1. Unit cell of the ASOW divided in subcells, which are the waveguide segments within the parallel dashed oblique lines. The subcells are modeled by the transfer matrices: \underline{T}_{1p} , \underline{T}_{1c} , \underline{T}_{2p} , and \underline{T}_{2c} . The transfer matrices \underline{T}_{ip} , with $i = 1, 2$ describe segments of the waveguide where the waves travel in three uncoupled waveguides, whereas \underline{T}_{ic} , with $i = 1, 2$, describe the coupling points, assumed to have zero thickness.

The matrices \underline{T}_{1p} and \underline{T}_{2p} are trivial.

$$\underline{T}_{1p} = \begin{pmatrix} e^{j\phi_a} & 0 & 0 & 0 & 0 & 0 \\ 0 & e^{-j\phi_a} & 0 & 0 & 0 & 0 \\ 0 & 0 & e^{j\phi_b} & 0 & 0 & 0 \\ 0 & 0 & 0 & e^{-j\phi_b} & 0 & 0 \\ 0 & 0 & 0 & 0 & e^{j\phi_a} & 0 \\ 0 & 0 & 0 & 0 & 0 & e^{-j\phi_a} \end{pmatrix} \quad (A1)$$

and

$$\underline{T}_{2p} = \begin{pmatrix} e^{j\phi_a} & 0 & 0 & 0 & 0 & 0 \\ 0 & e^{-j\phi_a} & 0 & 0 & 0 & 0 \\ 0 & 0 & e^{j\phi'_b} & 0 & 0 & 0 \\ 0 & 0 & 0 & e^{-j\phi'_b} & 0 & 0 \\ 0 & 0 & 0 & 0 & e^{j\phi_a} & 0 \\ 0 & 0 & 0 & 0 & 0 & e^{-j\phi_a} \end{pmatrix} \quad (A2)$$

but the matrices \underline{T}_{1c} and \underline{T}_{2c} demand a more careful consideration. They are

$$\underline{T}_{1c} = \begin{pmatrix} 0 & -j\frac{\tau}{\kappa} & \frac{j}{\kappa} & 0 & 0 & 0 \\ j\frac{\tau}{\kappa} & 0 & 0 & -\frac{j}{\kappa} & 0 & 0 \\ \frac{j}{\kappa} & 0 & 0 & -j\frac{\tau}{\kappa} & 0 & 0 \\ 0 & -\frac{j}{\kappa} & j\frac{\tau}{\kappa} & 0 & 0 & 0 \\ 0 & 0 & 0 & 0 & 1 & 0 \\ 0 & 0 & 0 & 0 & 0 & 1 \end{pmatrix} \quad (A3)$$

and

$$\underline{T}_{2c} = \begin{pmatrix} 1 & 0 & 0 & 0 & 0 & 0 \\ 0 & 1 & 0 & 0 & 0 & 0 \\ 0 & 0 & 0 & -j\frac{\tau}{\kappa} & \frac{j}{\kappa} & 0 \\ 0 & 0 & j\frac{\tau}{\kappa} & 0 & 0 & -\frac{j}{\kappa} \\ 0 & 0 & \frac{j}{\kappa} & 0 & 0 & -j\frac{\tau}{\kappa} \\ 0 & 0 & 0 & -\frac{j}{\kappa} & j\frac{\tau}{\kappa} & 0 \end{pmatrix}. \quad (\text{A4})$$

In the following we show how to obtain the transfer matrix \underline{T}_{1c} , with \underline{T}_{2c} being analogously derived. The transfer matrix \underline{T}_{1c} represents the infinitesimally thin (in z) segment with the top coupling point. As seen in Figure A1, there is no phase accumulation at the bottom ports (identified by the field amplitudes E_3^\pm). This explains the 2×2 identity matrix at the bottom right of \underline{T}_{1c} .

To model the change in the field amplitudes before and after the coupling point, we use a 4×4 scattering matrix, which gives the outputs in terms of the inputs. For the coupling point modeled in \underline{T}_{1c} , z_c , we have the following scattering matrix.

$$\begin{pmatrix} E_1^-(z_c^-) \\ E_2^-(z_c^-) \\ E_1^+(z_c^+) \\ E_2^+(z_c^+) \end{pmatrix} = \begin{pmatrix} 0 & \tau & 0 & -j\kappa \\ \tau & 0 & -j\kappa & 0 \\ 0 & -j\kappa & 0 & \tau \\ -j\kappa & 0 & \tau & 0 \end{pmatrix} \begin{pmatrix} E_1^+(z_c^-) \\ E_2^+(z_c^-) \\ E_1^-(z_c^+) \\ E_2^-(z_c^+) \end{pmatrix} \quad (\text{A5})$$

This 4×4 scattering matrix is transformed into the 4×4 transfer matrix embedded at the top left of the 6×6 \underline{T}_{1c} . The transformations are^[6]

$$\begin{aligned} \underline{T}_{11} &= \underline{S}_{21} - \underline{S}_{22} \underline{S}_{12}^{-1} \underline{S}_{11} \\ \underline{T}_{21} &= -\underline{S}_{12}^{-1} \underline{S}_{11} \\ \underline{T}_{12} &= \underline{S}_{22} \underline{S}_{12}^{-1} \\ \underline{T}_{22} &= \underline{S}_{12}^{-1} \end{aligned} \quad (\text{A6})$$

where each component, \underline{S}_{ij} and \underline{T}_{ij} , with $i, j = 1, 2$, is a 2×2 matrix that forms the 4×4 scattering and transfer matrices, respectively. The transfer matrix, which relates the field amplitudes at the left of the coupling point (z_c^-) with the field amplitudes at the right of the coupling point (z_c^+), is shown below.

$$\begin{pmatrix} E_1^+(z_c^+) \\ E_1^-(z_c^+) \\ E_2^+(z_c^+) \\ E_2^-(z_c^+) \end{pmatrix} = \begin{pmatrix} 0 & -j\frac{\tau}{\kappa} & \frac{j}{\kappa} & 0 \\ j\frac{\tau}{\kappa} & 0 & 0 & -\frac{j}{\kappa} \\ \frac{j}{\kappa} & 0 & 0 & -j\frac{\tau}{\kappa} \\ 0 & -\frac{j}{\kappa} & j\frac{\tau}{\kappa} & 0 \end{pmatrix} \begin{pmatrix} E_1^+(z_c^-) \\ E_1^-(z_c^-) \\ E_2^+(z_c^-) \\ E_2^-(z_c^-) \end{pmatrix} \quad (\text{A7})$$

Embedding this 4×4 transfer matrix on the top left of the 6×6 transfer matrix \underline{T}_{1c} , we obtain a full model of the infinitesimal segment with the top coupling point.

For the transfer matrix \underline{T}_{2c} , the coupling occurs for the field amplitudes E_2^\pm and E_3^\pm , so the 4×4 transfer matrix modeling the coupling point is embedded in the bottom-right part of the 6×6 \underline{T}_{2c} . As there is no change in E_1^\pm (due to the aforementioned infinitesimal thickness of the modeled segment), a 2×2 identity matrix goes at the top left. The rest of the matrix is filled with zeros.

The last step to obtain the transfer matrix is to right multiply the transfer matrix of each segment.

$$\underline{T}_u = \underline{T}_{2c} \underline{T}_{2p} \underline{T}_{1c} \underline{T}_{1p} \quad (\text{A8})$$

The full expression of \underline{T}_u is shown in Equation (5). The 6×6 transfer matrix \underline{T}_{aux} , which describes a modified unit cell without the bottom coupling to be used as a last cell, containing the output port, is similar to the transfer matrix \underline{T}_u but without right multiplying the matrix \underline{T}_{2c} , as

$$\underline{T}_{aux} = \underline{T}_{2p} \underline{T}_{1c} \underline{T}_{1p} \quad (\text{A9})$$

yielding

$$\underline{T}_{aux} = \begin{pmatrix} 0 & -j\frac{\tau}{\kappa} & j\frac{e^{j(\phi_a + \phi_b)}}{\kappa} & 0 & 0 & 0 \\ \frac{j\tau}{\kappa} & 0 & 0 & -j\frac{e^{-j(\phi_a + \phi_b)}}{\kappa} & 0 & 0 \\ j\frac{e^{j(\phi_a + \phi_b')}}{\kappa} & 0 & 0 & -j\frac{\tau e^{-j(\phi_b - \phi_b')}}{\kappa} & 0 & 0 \\ 0 & -j\frac{e^{-j(\phi_a + \phi_b')}}{\kappa} & j\frac{\tau e^{j(\phi_b - \phi_b')}}{\kappa} & 0 & 0 & 0 \\ 0 & 0 & 0 & 0 & e^{j2\phi_a} & 0 \\ 0 & 0 & 0 & 0 & 0 & e^{-j2\phi_a} \end{pmatrix} \quad (\text{A10})$$

Acknowledgements

This research was conducted with partial support from the Balsells Corporation Fellowship program that cosponsored A.H. from Spain to have the opportunity to conduct research and study in the USA at UC Irvine. This material was based upon work supported by the Air Force Office of Scientific Research award numbers LRIR 21RYCOR019 and FA8655-20-1-7052.

Conflict of Interest

The authors declare no conflict of interest.

Data Availability Statement

The data that support the findings of this study are available from the corresponding author upon reasonable request.

Keywords

frozen modes, serpentine optical waveguides, slow light, stationary inflection points

Received: December 22, 2021

Revised: April 8, 2022

Published online:

- [1] A. Figotin, I. Vitebskiy, *Laser Photonics Rev.* **2011**, 5, 201.
- [2] A. Figotin, I. Vitebskiy, *Waves Random Complex Media* **2006**, 16, 293.
- [3] R. Thomas, H. Li, M. Ellis, T. Kottos, *Phys. Rev. A* **2016**, 94, 043829.
- [4] M. Y. Nada, T. Mealy, F. Capolino, *IEEE Microw. Wirel. Compon. Lett.* **2021**, 31, 229.
- [5] G. Mumcu, K. Sertel, J. L. Volakis, I. Vitebskiy, A. Figotin, *IEEE Trans. Antennas Propag.* **2005**, 53, 4026.

- [6] M. Y. Nada, M. A. K. Othman, F. Capolino, *Phys. Rev. B* **2017**, 96, 184304.
- [7] B. Paul, N. K. Nahar, K. Sertel, *J. Opt. Soc. Am. B* **2021**, 38, 1435.
- [8] J. Scheuer, M. Sumetsky, *Laser Photonics Rev.* **2011**, 5, 465.
- [9] H. Ramezani, T. Kottos, R. El-Ganainy, D. N. Christodoulides, *Phys. Rev. A* **2010**, 82, 043803.
- [10] F. Yazdi, T. Mealy, A. Nikzamir, R. Marosi, F. Capolino, arXiv:2110.14095, **2022**, Unpublished.
- [11] H. Li, I. Vitebskiy, T. Kottos, *Phys. Rev. B* **2017**, 96, 180301.
- [12] N. Gutman, C. M. de Sterke, A. A. Sukhorukov, L. C. Botten, *Phys. Rev. A* **2012**, 85, 033804.
- [13] H. Ramezani, S. Kalish, I. Vitebskiy, T. Kottos, *Phys. Rev. Lett.* **2014**, 112, 043904.
- [14] M. B. Stephanson, K. Sertel, J. L. Volakis, *IEEE Microw. Wirel. Compon. Lett.* **2008**, 18, 305.
- [15] A. Figotin, I. Vitebskiy, *MRS Proc.* **2005**, 834, J1.2.
- [16] R. S. Knox, A. Gold, in *Lecture Notes and Supplements in Physics*, W.A. Benjamin Inc., New York **1964**.
- [17] J. Scheuer, O. Weiss, *Opt. Express* **2011**, 19, 11517.
- [18] A. Yariv, P. Yeh, in *Photonics: Optical Electronics in Modern Communications*, Oxford Series in Electrical and Computer Engineering, Oxford University Press, Oxford **2007**.
- [19] K. Vahala, in *Advanced Series in Applied Physics*, **2004**.
- [20] S. Fujita, K. Ito, in *Quantum Theory of Conducting Matter*, Springer, New York **2007**.
- [21] N. Apaydin, I. Zhang, K. Sertel, J. L. Volakis, *IEEE Trans. Microw. Theory Tech.* **2012**, 60, 1513.
- [22] M. A. K. Othman, V. A. Tamma, F. Capolino, *IEEE Trans. Plasma Sci. IEEE Nucl. Plasma Sci. Soc.* **2016**, 44, 594.
- [23] S. Axler, F. W. Gehring, K. A. Ribet, in *Calculus 1*, Springer, New York **1985**.
- [24] A. F. Abdelshafy, M. A. K. Othman, D. Oshmarin, A. T. Almutawa, F. Capolino, *IEEE Trans. Antennas Propag.* **2019**, 67, 6909.
- [25] K. Janocha, W. M. Czarnecki, *Schedae Inform.* **2017**, 25, 49.
- [26] Y. Dattner, O. Yadid-Pecht, *IEEE Photon. J.* **2011**, 3, 1123.
- [27] M. Cherchi, S. Ylinen, M. Harjanne, M. Kapulainen, T. Aalto, *Opt. Express* **2013**, 21, 17814.
- [28] A. Figotin, I. Vitebskiy, *Phys. Rev. E* **2005**, 72, 036619.
- [29] M. Veysi, M. A. K. Othman, A. Figotin, F. Capolino, *Phys. Rev. B* **2018**, 97, 195107.